Combined statistical-mechanistic modeling links ion channel genes to physiology of cortical neuron types

Yves Bernaerts[1,2,3], Michael Deistler[3,4], Pedro J. Gonçalves[3,4], Jonas Beck[1,2,3], Marcel Stimberg[5], Federico Scala[6], Andreas S. Tolias[6], Jakob Macke[3,4,7], Dmitry Kobak[1,2,3], and Philipp Berens[1,2,3,4,+]

[1]Hertie Institute for AI in Brain Health, University of Tübingen, 72076 Tübingen, Germany
[2]Institute for Ophthalmic Research, University of Tübingen, 72076 Tübingen, Germany
[3]Tübingen AI Center, 72076 Tübingen, Germany
[4]Department for Computer Science, University of Tübingen, 72076 Tübingen, Germany
[5]Sorbonne Université, INSERM, CNRS, Institut de la Vision, 75012 Paris, France
[6]Baylor College of Medicine, Houston, 77030, TX, USA
[7]Department of Empirical Inference, Max Planck Institute for Intelligent Systems, 72076 Tübingen, Germany
[+]Correspondence: philipp.berens@uni-tuebingen.de

ABSTRACT

Neural cell types have classically been characterized by their anatomy and electrophysiology. More recently, single-cell transcriptomics has enabled an increasingly finer genetically defined taxonomy of cortical cell types but the link between the gene expression of individual cell types and their physiological and anatomical properties remains poorly understood. Here, we develop a hybrid modeling approach to bridge this gap. Our approach combines statistical and mechanistic models to predict cells' electrophysiological activity from their gene expression pattern. To this end, we fit biophysical Hodgkin-Huxley models for a wide variety of cortical cell types using simulation-based inference, while overcoming the challenge posed by the model mismatch between the mathematical model and the data. Using multimodal Patch-seq data, we link the estimated model parameters to gene expression using an interpretable sparse linear regression model. Our approach recovers specific ion channel gene expressions as predictive of Hodgkin-Huxley ion channel densities, directly implicating their mechanistic role in determining neural firing.

1 Introduction

Neural cell types form the basic building blocks of the nervous system[1]. In the neocortex, they form intricate circuits giving rise to perception, cognition, and action[2–4]. Scientists have classically characterized these cell types by their anatomy or electrophysiology, and more recently, using molecular markers[3,5–7]. In the past decade, single-cell transcriptomics has enabled an increasingly finer genetically defined taxonomy of cortical cell types[8–11], but the link between the gene expression profiles of individual cell types and their physiological and anatomical properties remains poorly understood.

To tackle this question, the Patch-seq technique has been developed to combine electrophysiological recordings, single-cell RNA sequencing (scRNA-seq) and morphological reconstruction in individual neurons[12–15]. This approach has made it possible to directly study the relationship between the gene expression profile of a neural cell type and its physiological and anatomical characteristics. These studies have found that distinct subclasses of neurons (such as *Pvalb* or *Sst* interneurons, or intratelencephalic pyramidal neurons) show distinct physiological and anatomical properties[16,17]. Interestingly these properties seem to rather continuously vary within these subclasses, with few exceptions[17], possibly caused by smooth changes in gene expression.

This wealth of data has led to the development of sophisticated techniques for multi-modal data integration and analysis[18–21], but uncovering the *causal* relationships between e.g. transcriptomic and physiological properties of the neurons has been challenging. For example, sparse reduced-rank regression can reveal patterns of ion channel gene expression statistically predictive of particular expert-defined electrophysiological features[17], but precludes straightforward causal interpretation. Establishing mechanistic links experimentally is also challenging, as it involves genetic or pharmacological interventions.

Here, we argue that biophysical models of the physiological activity of neurons can help to close this gap as their parameters are explicitly interpretable. We constructed Hodgkin-Huxley (HH) models with single compartments[22–24] for the

electrophysiological activity of 955 neurons from adult mouse motor cortex (MOp) spanning various neural types and classes[17]. In contrast to the expert-defined features previously used to relate gene expression and physiological response patterns, the parameters of these models correspond to mechanistically interpretable quantities such as ion channel densities. We then developed a statistical method to predict HH parameters from the gene expression patterns of the same cells, providing a direct link between gene expression and electrophysiological activity with mechanistically interpretable latent quantities.

In order to find parameters of the mechanistic model that explain observed electrophysiology, we used simulation-based inference (SBI)[25,26]. This approach can recover the parameters of a mechanistic model based on summary statistics derived from model simulations, providing a posterior distribution over the model parameters. The posterior distribution allows to quantify the uncertainty in our model parameter estimates, in contrast to previous work using genetic algorithms[27,28]. As has been observed in other contexts[29–32], we found that SBI failed for our HH model and our data set due to a small but systematic mismatch between the data and the model, which could not be easily remedied by standard modifications to the HH model. We developed an algorithm that introduces noise to the summary statistics during training, which allowed it to perform reliable inference despite the model misspecification.

Using our improved SBI algorithm, we obtained posteriors over the HH parameters for all 955 neurons in our diverse data set. We found that parameter samples from the posterior provided for good model fits to the physiological firing patterns of most neurons, but observed higher parameter uncertainty in some subclasses such as *Vip* neurons. Furthermore, we showed that the relationship between gene expression patterns and the inferred HH model parameters could be learned using statistical techniques such as sparse reduced-rank regression, allowing to predict the electrophysiology of a cell from its gene expression across cortical neuron types and classes. Our approach recovered specific ion channel genes as predictive of HH model parameters corresponding to matching ion channel densities, directly implicating them in a mechanistic role for determining specific neuronal firing patterns that differ between cell types.

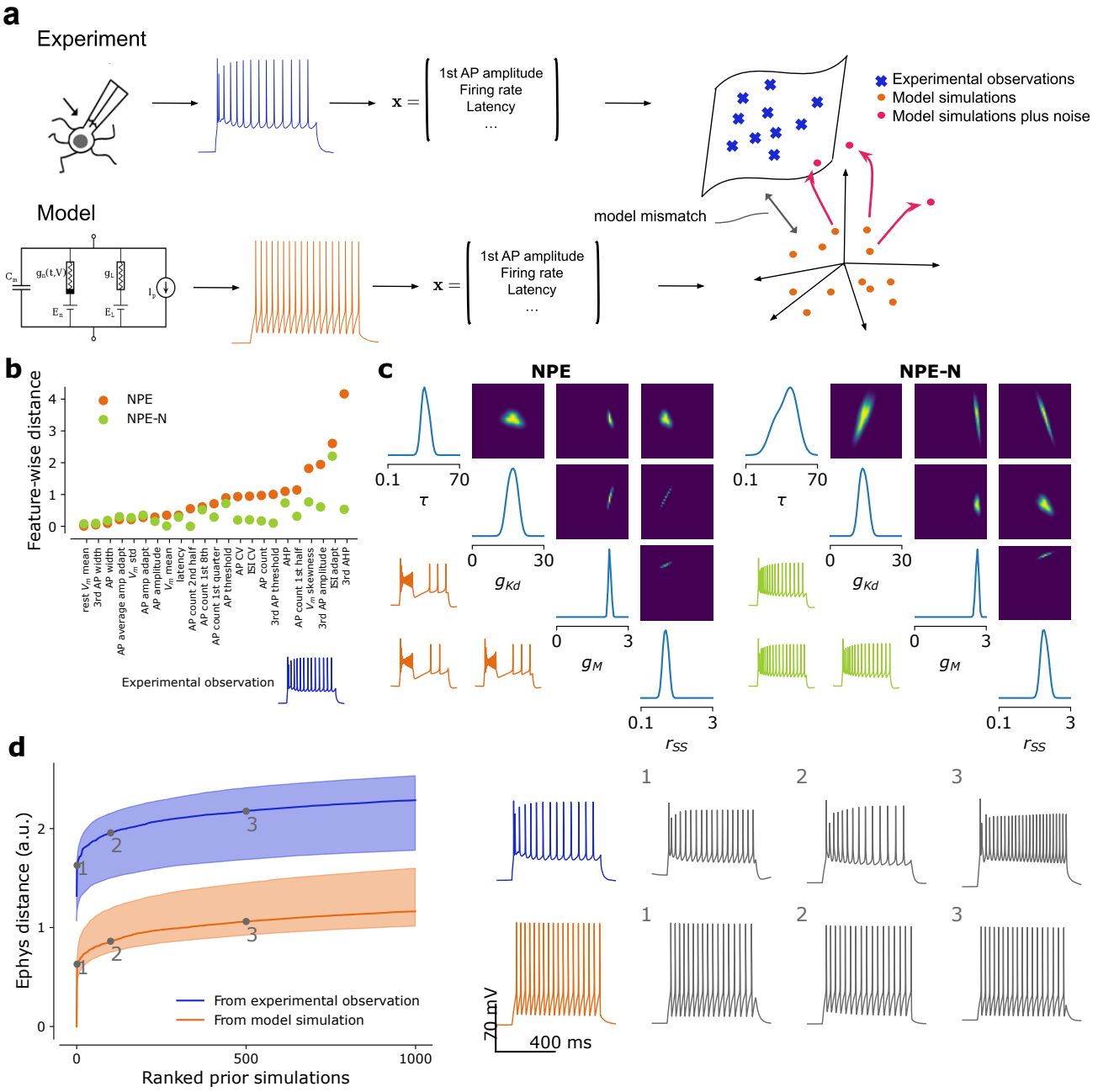

Figure 1 Simulation-based inference for Hodgkin-Huxley parameters in the presence of model misspecification. **a** Sketch illustrating model misspecification: in electrophysiological feature space, simulations do not cover the space of experimental observations. **b** The MAP parameter set simulation derived with NPE-N is closer to the experimental reference (in blue, below) than derived with NPE. Residual distance to reference shown for each electrophysiological feature (0 would denote perfect correspondence). **c** 1- and 2-dimensional marginals together with 3 simulations of highest posterior weight; NPE (left) vs NPE-N (right) setting. 4 out of 13 model parameters have been selected for illustration. **d** Simulations are further away from experimental observations (blue) than from other simulations (orange). Qualitatively, simulations increasingly further away from an experimental observation look more dissimilar than from another simulation. Numbers 1,2 and 3 refer to the 2nd, 101st and 501st closest simulations respectively.

2 Results

To better understand how the genetic identity of a cortical neuron determines its physiological activity, we studied a previously published data set of neurons from mouse motor cortex, which had been characterized with respect to their gene expression profile and electrophysiological properties using Patch-seq[17]. We focused on a subset of 955 cells which displayed action potentials to injection of a step current of $300pA$ and passed transcriptomic quality control. Each neuron expressed between 1202 and 18 118 genes with a mean expression of 7 245. The data set included 278 pyramidal neurons and 677 interneurons, consisting of 289 *Pvalb*, 240 *Sst*, 54 *Vip* and 11 *Sncg* neurons, using the cell subclasses and finer cell type labels assigned by the original authors based on mapping the gene expression patterns of the neurons to a larger reference atlas[11,17].

We hypothesized that we could further clarify the relationship between gene expression patterns and the electrophysiological response properties of the neurons, if we knew the mechanistically interpretable biophysical parameters underlying those. Therefore, we implemented a single-compartment HH model based on a previously established 'minimal' model that captures the electrophysiology in a wide range of neuronal subclasses[23]. We then increased the flexibility of our model with the addition of a small number of ion channels important for modeling pyramidal cells[24]. The parameters of the resulting model included passive parameters such as the capacitance and input resistance as well as active conductances of different ion channels or currents, which determine the physiological responses (Methods 4.2). Our final model included different sodium (Na^+), potassium (K^+), calcium (Ca^{2+}) and leak currents and had 13 free parameters overall, which needed to be inferred from the measured electrophysiological data (Methods 4.2).

To this end, we used neural posterior estimation (NPE)[25,33,34], an algorithm for SBI, which learns an approximate posterior distribution $q(\theta|\mathbf{x})$ over the parameter vector θ given a vector of features $\mathbf{x}$ computed from the data (Fig. 1a; Methods 4.4). The posterior distribution is parameterized as a sufficiently flexible neural network. In contrast to previous methods[27,28], this approach allowed us to quantify the uncertainty in the parameters after seeing the data.

We applied NPE to infer the 13 free parameters of our HH models given 23 features of the experimental recordings. These features included latency to the first spike, action potential count, amplitude and width or the membrane potential mean and variance (for a full list of all 23 features, see 4.3). We sampled 15 million parameter sets from a uniform distribution (the prior distribution) within biologically plausible ranges, ran the simulation for each of these parameter sets, computed the features of each of the simulated voltage traces, and trained NPE on the resulting synthetic data set. After training, the trained neural network can be evaluated on features of *any* experimental recording and returns the corresponding posterior distribution without further simulations or training.

However, this procedure did not work well for the neurons in our data set. In many cases, samples from the posterior or the maximum-a-posteriori (MAP) parameters did not produce simulations that came close to the experimental data (Fig. 1b, c) — on average 18% of posterior-sampled parameter sets produced simulations with at least one undefined summary feature, such as undefined latency due to a lack of action potentials (Table S1, standard NPE). Therefore, we further investigated the reason for this failure and found that the poor performance of the SBI pipeline was due to a systematic mismatch between the electrophysiological recordings and simulations from the model, a phenomenon recently observed also in other settings[29–32].

To show this, we selected a simulation from the synthetic data set of 15 million simulations and rank ordered all other simulations by their distance in the feature space to this reference (Fig. 1d). While few simulations were very close to the reference, most lay somewhat farther away, but still produced qualitatively very similar outcomes (Fig. 1d, orange). In contrast, if we chose an experimental trace as reference, the distance to the closest simulation in the electrophysiological feature space was larger than between any simulation from the synthetic data set (Fig. 1d, blue). Consequently, simulated traces were much more dissimilar to the experimental observations than to the simulated references.

From this analysis, we concluded that the experimental observations occupied a region of the electrophysiological feature space which was systematically shifted from the region occupied by the model simulations, despite our best efforts to create a HH model that has sufficient flexibility to capture the response diversity of the cortical neurons in our data set (Fig. 1a). For instance, we introduced the r_{SS} parameter to the model (Methods 4.2), that can scale the speed with which ion channels reach open steady states, in order to alleviate model-data mismatches observed in the action potential width. Although this approach substantially reduced overall model misspecification, it did not remove it entirely (Fig. S1). As a consequence, many simulations produced with randomly drawn posterior samples had either one or more undefined electrophysiological feature or found themselves at a large distance to their experimental reference (Fig. 1b, c left; Table S1).

We found that modifying the estimation algorithm improved the performance of the inference procedure despite the model mismatch. We smoothed the feature space by adding a small amount of independent Gaussian noise to the electrophysiological features of selected simulations close to the experimental observations and used those to train the neural density estimator (Methods 4.5). This procedure yielded posterior simulations which came much closer to their experimental reference both qualitatively and quantitatively (Fig. 1b,c; distance in electrophysiological feature space $\|\mathbf{x_{MAP}} - \mathbf{x_o}\|_2 = 4.35 \pm 2.86$ vs. $\|\mathbf{x_{MAP}} - \mathbf{x_o}\|_2 = 6.24 \pm 3.24$, NPE-N vs. NPE, mean $\pm$ SD, Table S1). We experimented with different strategies including different magnitudes of noise and chose a compromise between simulations from the posterior being close to the measured data

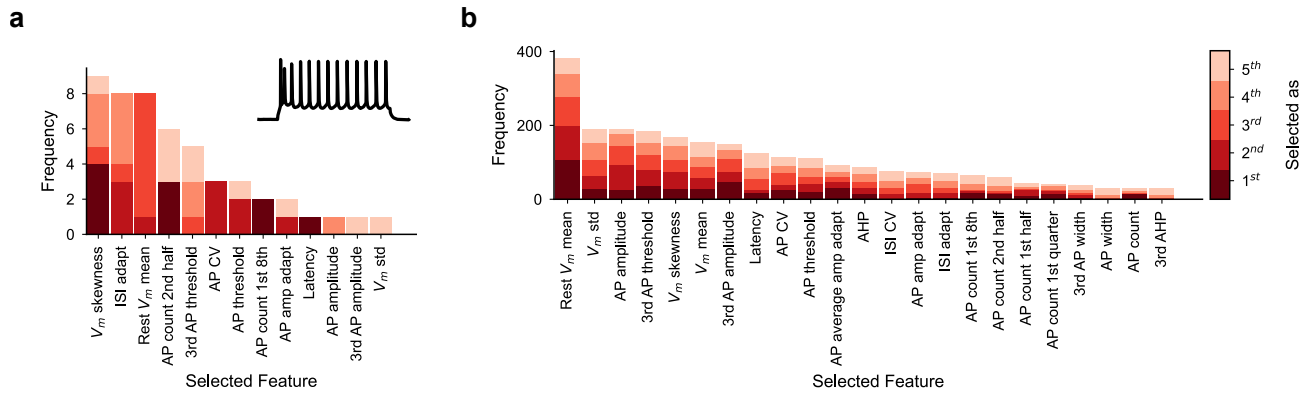

Figure 2 Ranking commonly used electrophysiological features by their ability to constrain posterior estimates. a Features are ranked by how often they are strongly constraining the posterior of a Pvalb neuron. Strongly constraining features minimize the KL divergence between posterior estimates subject to all 23 features and estimates considering only five. Important features were selected across 10 repeated runs. Shading indicates the order in which they are selected as part of the top five. Features are ranked in descending order. **b** Summary across all 955 MoP neurons, of which features are strongly constraining the posterior estimates.

and a low fraction of simulations that result in undefined features (Methods 4.5). We called the resulting procedure NPE-N and used it to obtain posterior distributions over parameters for all 955 neurons in our data set.

To gain further insights into the inference procedure, we next wondered which out of the 23 features were most important to constrain the posterior. To this end, we used an algorithm that efficiently compares a posterior constrained by the full set of features to one constrained by a growing subset of features[35] and studied a subset of 50 neurons (Methods 4.6). We ran this algorithm five times for each of these neurons, and counted how often a feature was selected as one of the five most important features (Fig. 2a). We then compiled the results of this selection procedure across all 50 neurons that we investigated and found that on average, the mean resting membrane potential was by far the single most important feature, followed by the mean potential during current stimulus, action potential amplitude, the action potential threshold and the variance of the membrane potential (Fig. 2b).

We next returned to our original question and studied how the transcriptomic identity of the neurons in our data set was related to their electrophysiological properties and the parameters of the best fitting HH model. To this end, we created a two-dimensional visualization of the gene expression data for all 955 MoP neurons (Fig. 3a). We assigned colors based on the mapping of the individual neurons to the transcriptomic types identified in a reference atlas[11,17]. We found that the resulting embedding separated the major neural subclasses very well including interneurons and pyramidal neurons (Fig. 3a). We confirmed the identity of these subclasses by overlaying the expression strength of various marker genes such as *Pvalb*, *Sst*, *Vip* and *Lamp5* (Fig. 3b). Furthermore, the posteriors for neurons from some subclasses were less constrained than those of others, indicated by higher posterior uncertainty (Fig. 3c). Specifically, this affected Vip neurons, which were relatively sparsely sampled in the data set. In contrast, Pvalb neurons showed lowest uncertainty indicating that their posteriors were best constrained using the available features given the current HH model. One reason for this may be that Pvalb neurons fired more stereotypically, whereas Vip neurons showed greater variability in their firing patterns[17,36], that may require greater flexibility in the model to reproduce all summarizing statistics.

We overlaid the individual electrophysiological features on this two-dimensional embedding, both for the experimentally measured data and for simulated MAP traces (Fig. 3e and f). We found that these features varied strongly between neural subclasses, as expected, and that the features extracted from simulated traces matched the features from measured traces overall very well: for example, pyramidal neurons showed higher action potential amplitude and width as well as lower spike rates, in line with the observations. For some features, such as the latency of the response, the match was less perfect, as the simulated traces of interneuron subclasses had overall higher latency than those experimentally measured.

Next, we studied how the parameters of the HH model varied across this transcriptomically defined embedding (Fig. 3d). This visualization allowed us to reason about the relationship between biophysical parameters and the resulting electrophysiological properties in some of the genetically defined subclasses. For example, the conductivity of the delayed rectifier potassium current $\overline{g}_{Kd}$[37] was estimated to be high for *Pvalb* interneurons (Figure 3d), suggesting that these currents were important for quickly repolarizing the membrane potential $V_m(t)$ during AP generation in order to obtain the small *AP widths* and high *AP count* of fast-spiking *Pvalb* cells (Figure 3d-f). Likewise , the membrane time constant τ and the scaling parameter r_{SS} seem

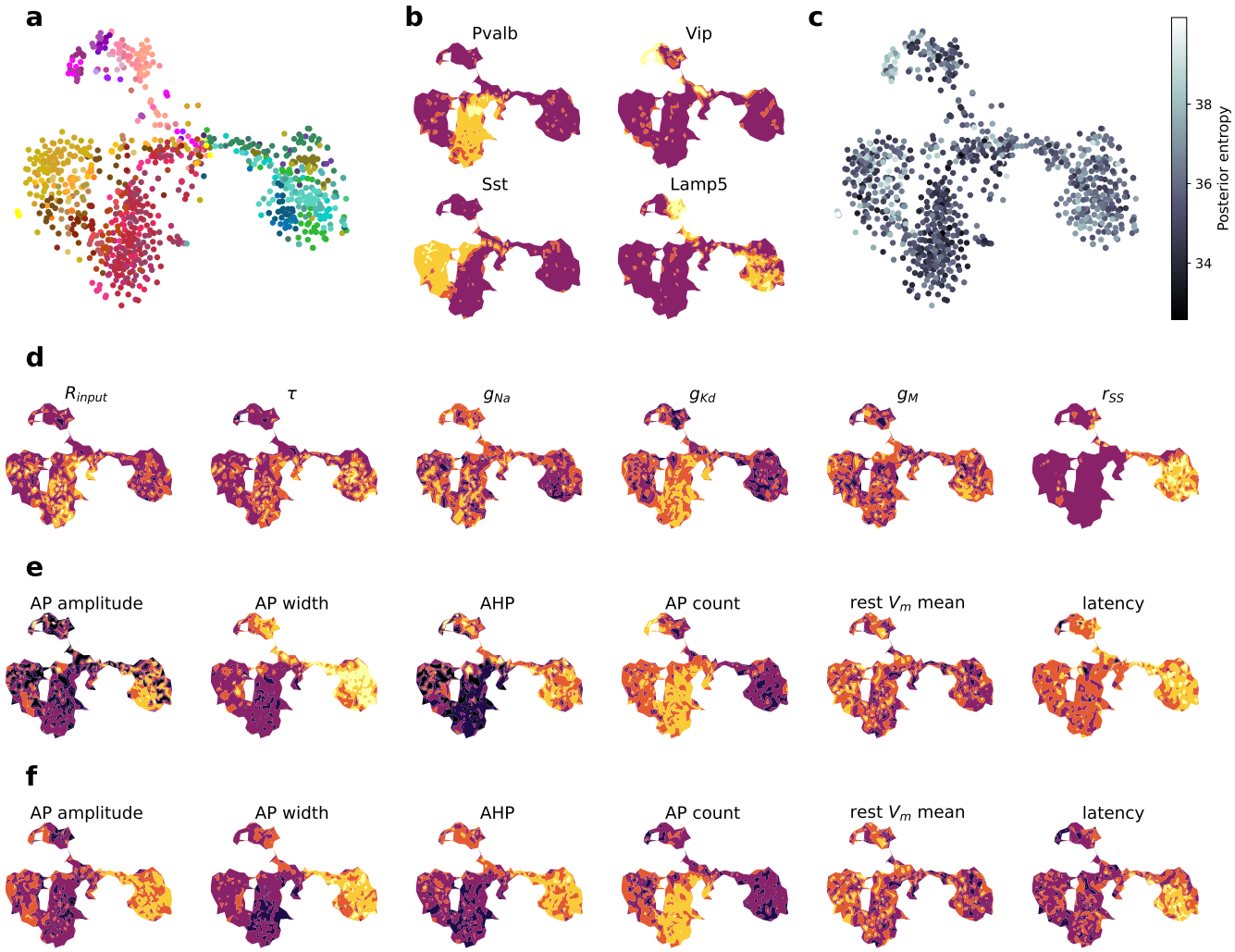

Figure 3 Two-dimensional embedding of 955 MoP neurons reveals difference in HH parameters between neural families. **a** T-SNE embedding of $n = 955$ Mop neurons based on transcriptomic data. *Pvalb* (red), *Sst* (yellowish), *Vip* (purple) and *Lamp5* (pink) and secondly excitatory Pyramidal *Pyr* neurons (blue-and greenish). Cells in the middle of the embedding tend to show lower quality transcriptomic data and therefore group together. **b** Marker genes expression levels overlayed and interpolated on embedding confirm known subclasses (dark purple: low expression, yellow: high). **c** Uncertainty of MAP parameters for each cell overlayed on the embedding. The uncertainty was calculated as the posterior entropy $\sum_{k=1}^{1000} -\log q_\phi(\theta_k \mid \mathbf{x}_o)$, where we sampled $\theta_k \sim q_\phi(\theta \mid \mathbf{x}_o)$. **d** Selection of MAP parameters, overlayed on embedding. **e** Selection of summary statistics derived from simulations corresponding to MAP estimates, overlayed on embedding. **f** Selection of summary statistics describing observed electrophysiology, overlayed on embedding.

important to fit the large action potential widths and high latency observed for pyramidal neurons (Figure 3d-f).

Given these results, we were now in a position to quantitatively study the relationship between the transcriptomic identity of a neuron and its biophysical parameters. To this end, we trained a linear sparse reduced-rank regression model (sRRR)[18] and a non-linear sparse bottleneck neural network (sBNN)[19] to predict the biophysical parameters ($d = 13$) from the gene expression data (Fig. 4a). To ease the interpretability, we focused on ion channel and known marker genes only ($d = 427$) and trained linear and non-linear models with a two-dimensional latent space. We found that model parameters could be predicted with reasonable accuracy (sRRR: $R^2 = .17 \pm 0.03$, mean $\pm$ SD across cross-validation folds, for a model selecting approximately 25 genes) and that the non-linear model performed just as well as the linear one (sBNN: $R^2 = 0.17 \pm 0.03$), so we analyzed only the linear model further (Fig. 4b). Using the entire data set, this model predicted some parameters such as the conductance of the voltage dependent or delayed rectifying potassium current ($\overline{g}_{KV31}$ and $\overline{g}_{Kd}$) or the membrane capacitance C particularly well (Fig. 4c). Other model parameters were less well predicted, such as the leak current E_{leak} or the muscarinic potassium channel $\overline{g}_M$. Interestingly, the r_{SS} parameter was predicted best, which we introduced as a first step towards alleviating model

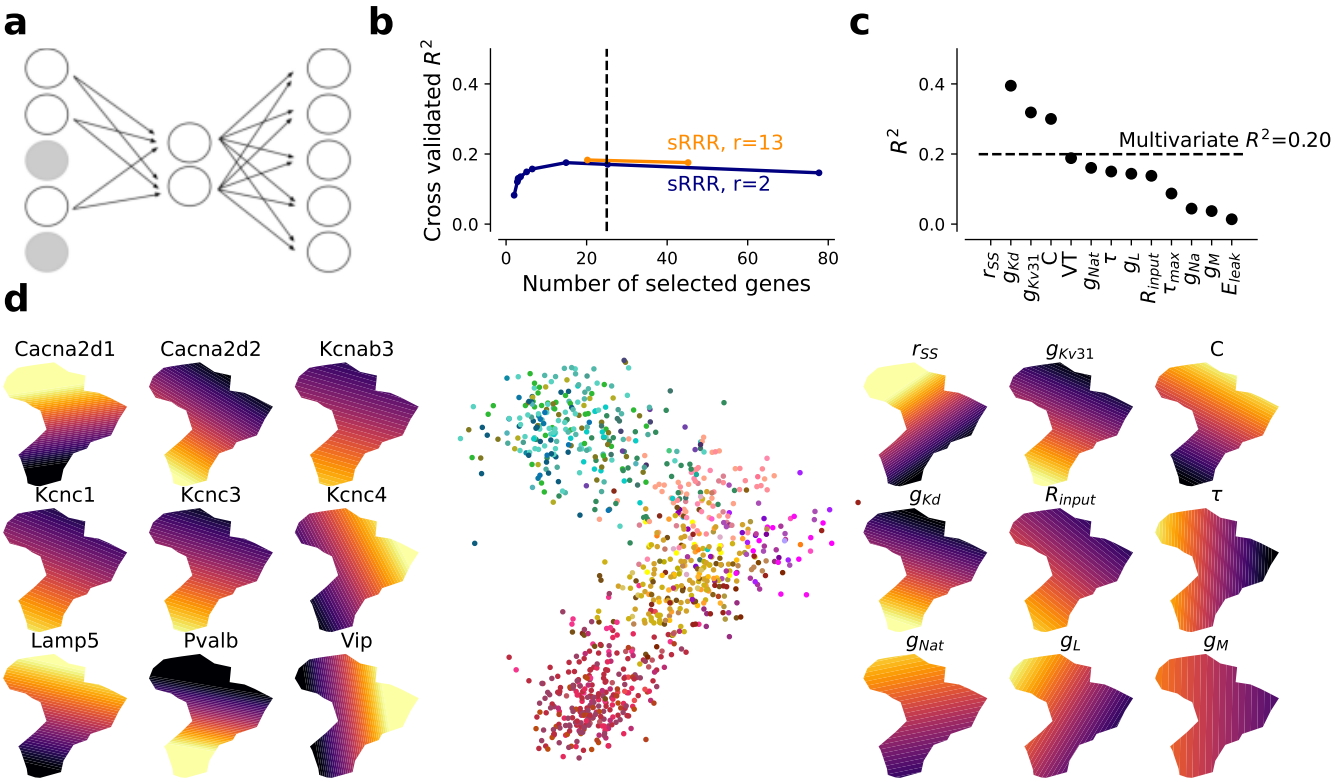

Figure 4 Prediction of MAP parameter estimates from gene expression with sparse reduced-rank regression. a SRRR schematic. **b** Cross-validation performance for rank-2 and full rank sRRR models with elastic net penalty. The dashed vertical line shows the performance with 25 genes. **c** Rank-2 sRRR model predictive performance for each model parameter, using the entire data set. **d** Middle: rank-2 sRRR model latent space visualization. All 955 MoP neurons are shown. Left: Selected ion channel and marker gene overlays. Right: Predicted model parameter overlays.

mismatch issues.

We visualized the latent space of the sRRR model to better understand the relationship between ion channel and marker genes and the HH model parameters (Fig. 4d). This embedding is conceptually similar to the t-SNE visualization of the entire gene space with overlayed model parameters and electrophysiological properties (Fig. 3), except that we here focus on genes that predict HH model parameters. The 2D latent space of the sRRR model showed two principal directions of variation, where one separated pyramidal cells from interneurons and the other mostly different interneuron subclasses. In addition, we found that the sRRR model identified mechanistically plausible relationships: for example, the potassium channel conductances $\overline{g}_{Kv31}$ and $\overline{g}_{Kd}$ were both high in *Pvalb* neurons placed in the lower left corner, predicted by the expression of various potassium channel genes like *Kcnc1*, that constitutes a subunit of the Kv3.1 voltage-gated potassium channel, and *Kcnab3* respectively. Likewise, the calcium channel conductance $\overline{g}_L$ was predicted by high expression of *Cacna2d1* that directly encodes for the alpha-2 and delta subunits in the L-Type calcium channel. Our sRRR model selected *Cacna2d2* as well, which is a paralog gene with opposite expression to *Cacna2d1* (Fig. 4d, left). In addition, classical marker genes like *Vip* acted as surrogate cell subclass markers and contributed to the prediction.

This approach can be used to accurately predict HH models for neurons for which we only measured gene expression but not electrophysiology. The models predictions captured essential variation in the model parameters both on the subclass and the cell type level (Fig. 5a, b), such that model simulation with these parameters showed very similar firing patterns as representative examples from the subclasses (Fig. 6).

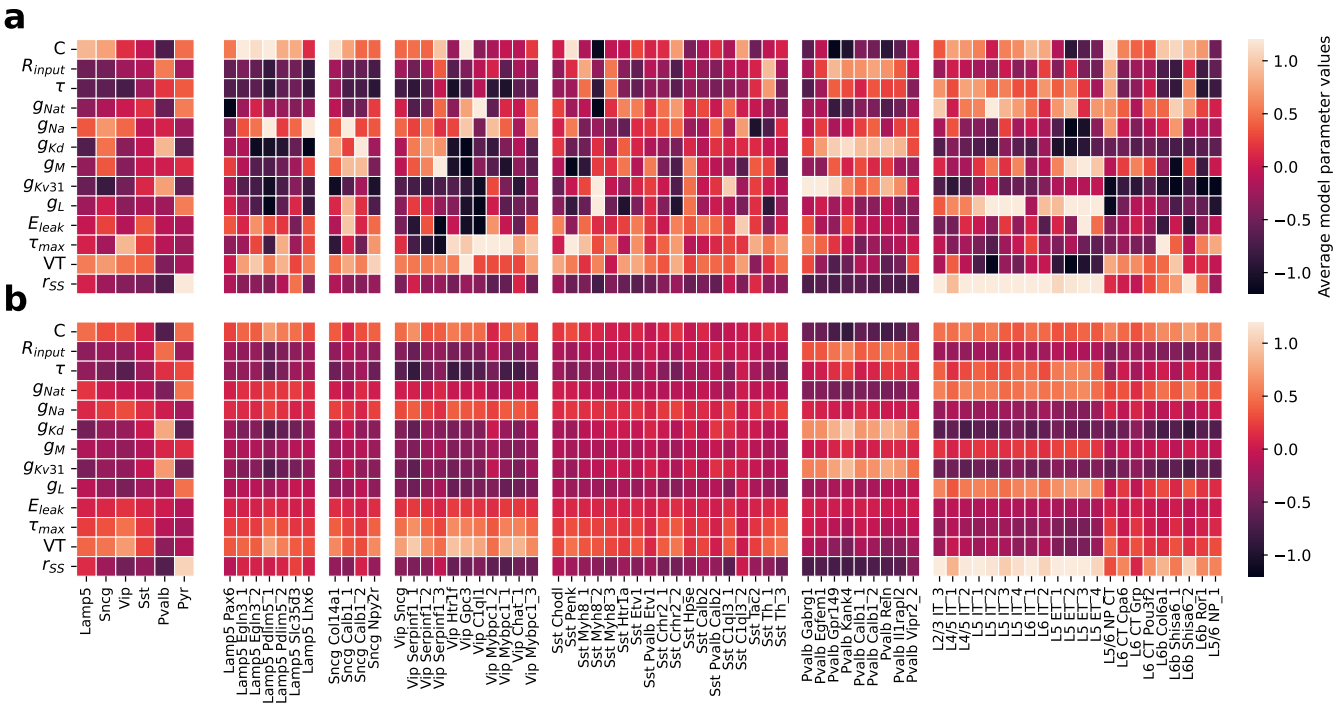

Figure 5 MAP parameter estimates and sRRR predictions for each subclass and cell type. a MAP parameter estimates averaged over cells belonging to a family and belonging to a transcriptomic cell type (left and right respectively). Estimates are Z-scored. **b** Analogous to a, but with rank-2 sRRR predicted model parameter values.

3 Discussion

In this study, we directly linked the gene expression profile of a set of cortical neurons to HH model parameters fitted to their electrophysiological signatures. We believe this is a major step towards closing the "causality" gap between gene expression and neural physiology: In previous work, we and others have simply correlated gene expression and electrophysiology, e.g. predicting electrophysiological properties from transcriptomic data[17–21], but uncovering the causal relationships between these quantities has been challenging.

The mechanistic HH model we used here spells out our causal understanding of how electrophysiological properties arise from ion channel densities and other passive properties of a neuron,leaving the link between these quantities and the expression of certain genes to be explained by a statistical model.In our approach, we used a linear reduced-rank regression model with groupwise sparsity constraint on the genes, selecting genes in or out of the model based on the available data. Given the present data, we found that the linear model with a two-dimensional intermediate layer performed as well as a comparable non-linear model. Partially, this may be due to the noise in gene expression and the comparably small data set, but it is also possible that our explicit mechanistic model for the generation of electrophysiological activity explained away some of the nonlinear relationship between gene expression and electrophysiological features. Larger data sets will likely also help the linear model to resolve better observed differences in model parameters between fine cell types, which are currently captured only to a certain extend (Fig. 5).

Previous work has also attempted to infer biophysical parameters in HH models and link the inferred values to neural cell classes and their gene expression[23,24,27,28]. This work differed from ours in that most of these studies did not directly link parameters in HH models to the expression of a large set of genes, but rather studied on HH parameter differences between genetically defined cell classes[23,24,27]. One recent study examined the relationship between HH parameters and individual genes[28], but did not provide a systematic statistical model for this link. Also, none of these studies used uncertainty aware parameter inference techniques. Incorporating uncertainty allowed us to highlight cells, cell types or classes for which the inference procedure returned results which were not as well constrained by the data.

Nevertheless, many trends in model parameters across different cell classes matched previous observations qualitatively. For instance, we found that different values are needed for the potassium conductance $\overline{g}_{Kv3.1}$ to model *Vip*, *Sst* and *Pvalb* neurons and that the expression of *Kcnc1* varies accordingly (Fig. 4d). In a similar vein, Nandi et al. report different values for $\overline{g}_{Kv3.1}$ and show that *Kcnc1* is differentially expressed between these classes[28]. In their work, this example is hand-selected

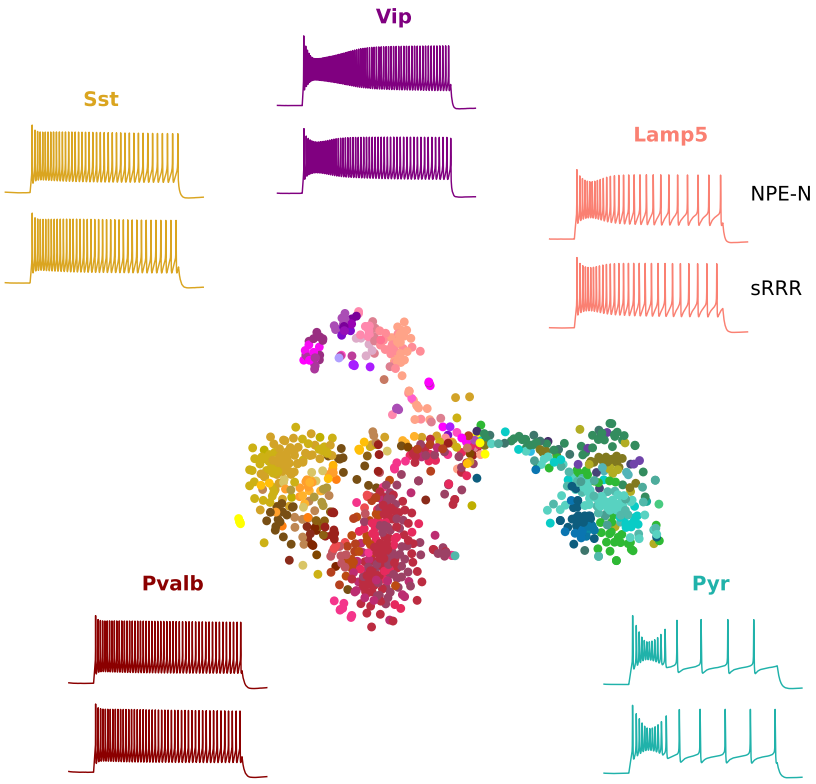

Figure 6 Subclass representation of MAP estimates together with sRRR predictions. T-sne embedding as in Fig 3a. Simulation on top is derived from the subclass MAP estimate calculated as in Fig. 5a, left. Simulation on the bottom is derived from the subclass sRRR prediction calculated as in Fig. 5a, left.

for analysis, while in our analysis the evidence emerges from the sRRR model. While not all correspondences with other studies are as close as this, HH models show redundancy in their parametrizations[25,38,39], such that different model parameter combinations can result in similar responses, potentially explaining observed deviations.

Our biological question to identify a quantitative link between gene expression and electrophysiological activity patterns led us to devise a methodological innovation to overcome the challenges posed by systematic mismatch between our simulations and the experimental data, which caused the out-of-the-box simulator-based methods to fail. We achieved this by adding noise to the summary statistics derived from the simulations, effectively smoothing the feature space. In parallel work to this paper, this phenomenon has recently received more widespread attention[29–32]: for instance, robust neural posterior estimation[29] takes the opposite approach to our strategy and denoises the measured data towards the model using Monte-Carlo sampling. On the other hand, robust synthetic likelihood approaches[40] that estimate likelihoods rather than posteriors, work similarly to our approach. Which strategy works best for which models and circumstances remains to be evaluated, but these strategies will allow to apply simulator-based inference techniques in cases where models provide relatively coarse, but useful approximations of the true phenomena. Alternatively, one could make the model more realistic. In our case, some of the model mismatch is likely also caused by the use of single-compartment models in contrast to other studies, which used HH models with two or more compartments[24,27,28], however, such complex models are currently difficult to use with simulation-based inference.

Mechanistic models that make biophysical processes explicit are ultimately desirable all the way from gene expression to electrophysiology, as such models form the highest level of causal understanding[41]. To further close this "causality" gap would require an explicit mechanistic model for the translation of mRNA into proteins such as ion channels — a relationship, which is all but simple[42–44]. Mechanistic models for this process have been suggested in the literature on a variety of scales[45,46], but it is an open question how such models could be integrated in the inference procedure given the temporal and spatial processes involved in mRNA translation[45–47]. While directly measuring translation dynamics in live cells has become possible using

live cell imaging approaches[48,49], it remains an extremely challenging task, especially in multicellular systems and given the diversity of cortical neurons. Therefore, the combination of machine learning-based models with explicit mechanistic models may provide a viable path forward to improve our understanding of neuronal diversity even if we do not have full causal empirical knowledge of the entire chain of events, aiding the inference of important intermediate quantities.

4 Methods

4.1 Data Set

We reanalyzed a published data set consisting of $n = 1328$ adult mouse motor cortex (MOp) neurons[17], which had been characterized transcriptomically and electrophysiologically using Patch-seq. We downloaded the read count data from https://github.com/berenslab/mini-atlas and the electrophysiological traces from https://dandiarchive.org/dandiset/000008. The authors used Smart-seq2 to obtain single-cell transcriptomes for these neurons. Out of $n = 1328$ cells, $n = 1213$ cells passed transcriptomic quality control and were assigned a transcriptomic cell type using the 1000 genes that were most variable across this subset of cells. For electrophysiological characterization, the authors injected negative to positive constant currents for 600 ms time windows starting at -200 pA with steps of 20 pA to positive currents beyond 400 pA or until the cell died. Electrophysiological experiments were performed at a temperature of 25 $°C$. For further experimental details, see[17]. Finally, out of $n = 1328$ cells, we analyzed $n = 955$ cells that had well-defined summary statistics in their membrane voltage response to current injection of 300 pA.

4.2 Hodgkin-Huxley Model

We used a single-compartment HH model[23] that was designed to reproduce electrophysiological behavior of a wide variety of neurons across species with a minimal set of ion channels. To account for the variability across excitatory and inhibitory cortical neurons, we added additional ion channels[24] and introduced r_{SS}, a parameter influencing how rapid gates reach open and closed steady states in some sodium and and potassium currents. Without these modifications we could not fit wider *AP widths* observed in Pyramidal cells.

The HH model solves the following ODE $V_m(t) = f(V_m(t), \theta)$ for $V_m(t)$, the membrane voltage as a function of time:

$$
\begin{aligned}
\frac{dV_m(t)}{dt} &= \frac{1}{C}\left(I_{Na} + I_{Nat} + I_{Kd} + I_M + I_{Kv3.1} + I_L + I_{leak} - I_{inj} - I_{noise}\right) \\
I_{Na} &= \overline{g}_{Na}\, m^3\, h\, \left(E_{Na^+} - V_m(t)\right) \\
I_{Nat} &= \overline{g}_{Nat}\, \hat{m}^3\, \hat{h}\, \left(E_{Na^+} - V_m(t)\right) \\
I_{Kd} &= \overline{g}_{Kd}\, n^4\, \left(E_{K^+} - V_m(t)\right) \\
I_M &= \overline{g}_M\, p\, \left(E_{K^+} - V_m(t)\right) \\
I_{Kv3.1} &= \overline{g}_{Kv3.1}\, v\, \left(E_{K^+} - V_m(t)\right) \\
I_L &= \overline{g}_L\, q^2\, r\, \left(E_{Ca^{2+}} - V_m(t)\right) \\
I_{leak} &= \overline{g}_{leak}\, \left(E_{leak} - V_m(t)\right).
\end{aligned}
$$

Here, $\overline{g}_x$ and E_x denote the maximum channel conductance and reversal potential of membrane ion channel x respectively. C is the membrane capacitance and $I_{inj} = 300pA$ denotes the magnitude of experimental current injected between current stimulation onset at 100 ms and stimulation offset 700 ms. In order to model small membrane voltage fluctuations observed experimentally, we further introduced Gaussian current noise $I_{noise} \sim \mathcal{N}(10, 1)$ at every time point.

Furthermore, ion channel activation and inactivation gates follow dynamics $\frac{dx}{dt} = \alpha_x(V_m(t))\,(1-x) + \beta_x(V_m(t))\,x$, where $x \in \{m, h, \hat{m}, \hat{h}, n, p, v, q, r\}$. Opening α_x and closing β_x rate constants depend on the membrane voltage $V_m(t)$ as previously described[23,24]. In order to account for the 25 $°C$ temperature at which Patch-seq experiments were performed, we used a temperature coefficient $Q_{10} = 2.3$ to scale the kinetics with which gates in ion channels open and close. Parameter r_{SS}, further scales the rates with which sodium and potassium currents with maximal conductances $\overline{g}_{Na}$ and $\overline{g}_{Kd}$ reach steady states.

In total, 13 parameters in the model can be tuned in order to fit observed electrophysiology of $n = 955$ MOp cells (Table 1 for details). We implemented the model with the `Brian2` toolbox[50] in `Python`, which can efficiently transpile and simulate models in C++.

In order to understand the significance of adding the r_{SS} in reducing model misspefication on a "model implementation" level rather than training the density estimator, we compared to the same HH model but with scaling parameter $r_{SS} = 1$ (Fig. S1).

Model parameter	Prior range	Description
C	$[0.1, 15]\ \frac{\mu F}{cm^2}$	The membrane capacitance C measures how much charge can be stored per voltage difference V_m across the membrane.
R_{input}	$[20, 1000]\ M\Omega$	The input resistance R_{input}, equals the membrane voltage V_m deflection from resting state divided by injected current. The inverse is called the leak conductance g_{leak}.
τ	$[0.1, 70]\ ms$	Here, τ describes the time for the membrane potential to *increase* by a fraction of $(1-1/e)$, or 63 %, from its resting membrane state during the application of the positive 300 pA current pulse.
$\overline{g}_{Nat}$	$[0, 250]\ \frac{mS}{cm^2}$	Maximal conductance of the fast inactivating Na^+ current[24,51].
$\overline{g}_{Na}$	$[0, 100]\ \frac{mS}{cm^2}$	Maximal conductance of the Na^+ current[23,37].
$\overline{g}_{Kd}$	$[0, 30]\ \frac{mS}{cm^2}$	Maximal conductance of the delayed rectifier K^+ current[23,37].
$\overline{g}_{M}$	$[0, 3]\ \frac{mS}{cm^2}$	Maximal conductance of the slow non-inactivating *muscarinic* K^+ current[23,52].
$\overline{g}_{Kv3.1}$	$[0, 250]\ \frac{mS}{cm^2}$	Maximal conductance of the fast non-inactivating K^+ current[24,53].
$\overline{g}_{L}$	$[0, 3]\ \frac{mS}{cm^2}$	Maximal conductance of the high-threshold Ca^{2+} current[23,54].
E_{leak}	$[-130, -50]\ mV$	Reversal potential of the leak current.
τ_{max}	$[50, 4000]\ ms$	Time constant describing how rapid the *muscarinic* current channel opens (see g_M).
V_T	$[-90, -35]\ mV$	Parameter that can adjust the AP threshold.
r_{SS}	$[0.1, 3]$	Rate to steady state (SS). Parameter introduced to change how rapid gates reach open and closed steady states in Na^+ current with maximal conductance $\overline{g}Na$ and K^+ current with maximal conductance $\overline{g}_{Kd}$.

Table 1 Description of the 13 HH-model parameters.

4.3 Electrophysiological Features

We automatically extract 23 electrophysiological summary features from the measured or simulated voltage traces $V(t)$ using a Python library from the Allen Software Development Kit (SDK) (https://github.com/AllenInstitute/AllenSDK) with modifications to account for our experimental paradigm (https://github.com/berenslab/EphysExtraction, Table 2).

4.4 Standard Neural Posterior Estimation

Standard NPE applied to HH models starts off by sampling HH model parameter sets from a prior distribution $\theta \sim p\theta$, followed by creating synthetic data sets through the simulator or HH model, and eventually trains a deep neural density estimator $q_\phi(\theta \mid \mathbf{x})$, a neural network, to learn the probabilistic association between summary statistics $\mathbf{x}$ derived from simulations and its parameter sets θ. Experimental observations $\mathbf{x_o}$ can then be fed to the density estimator in order to derive all parameter sets consistent with the data and the prior, i.e. the posterior distribution $q_\phi(\theta \mid \mathbf{x}_o)$[25].

We used the sbi toolbox https://www.mackelab.org/sbi/ to run NPE with different training schedules, including NPE-N, which we explain in the next section.

4.5 Dealing with Model Mismatch in Neural Posterior Estimation

Posterior distributions derived with standard NPE can suffer from model mismatches, that is, when simulations generally fail to adequately cover experimental observations in summary statistic or electrophysiological space. They can become confidently wrong, placing high posterior weight on parameter sets that do not reproduce experimental recordings and low posterior weight to parameter sets that do (Fig. 1). In machine learning jargon, the trained density estimator fails to extrapolate to experimental observations (test data) which are outside of the distribution of the training data.

We experimented with various modifications of NPE in order to make the posterior more robust to the mismatch between model and experimental observations. First, we tried to include only simulations which position themselves close to experimental observations in summary statistic space (Table S1, *Best Euclidean*). Closeness was measured by calculating the Euclidean distance between simulation and observation after standardizing all summary statistics. Second, we introduced different levels

of isotropic Gaussian noise to the summaries of those simulations (Table S1, *Add x amplitude noise to ephys*). Third, besides adding noise to summary statistics, we introduced isotropic Gaussian noise to the model parameters with which the close simulations were generated (Table S1, *Add 0.05 amplitude noise to ephys and model parameters*). Finally, we experimented with a mixture of non-manipulated close simulations and close simulations with noise added to their summary statistics (Table S1, *Data augmentation*).

Given their performance measures (Table S1), we decided to use NPE with added isotropic Gaussian noise only to the summary statistics of simulations close to experimental observations in summary statistic space. We call the method NPE-N. The noise is of moderate amplitude such that a tradeoff is established between closeness of simulations of MAP estimates to the experimental observations with closeness of simulations from random posterior samples (Table S1, 3rd and 4th column).

In contrast to NPE, NPE-N produced posteriors that give high posterior weight to model parameter sets that both qualitatively and quantitatively produce simulations close to experimental observations.

4.6 Feature Selection through Likelihood Marginalization

To analyze which features were informative for constraining the inference procedure, we used Feature Selection through Likelihood Marginalization[35] (FSLM). To ensure comparable posterior estimates between FSLM and NPE, we trained FSLM with 3 million spiking simulations randomly generated from the prior to which we also introduced isotropic Gaussian noise in their summary statistics. We then drew 1000 samples from the posteriors of each observation x_o, for 5 different initializations of FSLM and only selected the 50 experimental observations with smallest average $KL(p_{NPE-N}(\theta \mid x_o) | p_{FSLM}(\theta \mid x_o))$[55] for feature selection. The final ranking was derived from 1000 samples per posterior and is averaged across 10 initializations.

4.7 Visualization

We used the `openTSNE` implementation with default parameters (https://github.com/pavlin-policar/openTSNE) to embed the transcriptomic space with t-SNE to a final two-dimensional representation with default parameters.

4.8 Sparse Reduced-Rank Regression and sparse Bottleneck Neural Networks

To link gene expression data to HH model parameters, we used a linear sparse reduced-rank regression[18]. This framework reduces the high-dimensional gene space data to a 2-dimensional latent (rank=2), which is maximally predictive of the HH parameters. An elastic net penalty was used to select the most relevant genes. As a nonlinear extension to sRRR we also tested the use of sparse bottleneck neural networks (sBNN), that utilize a neural network with bottleneck to predict electrophysiological measurements from transcriptomic space[19]. Analogously to sRRR, a group lasso penalty was used on the weights of the first layer to select most meaningful genes.

Electrophysiological feature	Description
AP threshold	Membrane voltage at the time where the first derivative of the voltage w.r.t. time reaches a threshold, which elicits the first AP.
AP amplitude	Height of the 1st AP, measured from threshold to maximum voltage.
AP width	Width at half height of the 1st AP
AHP	Afterhyperpolarization. Depth of the membrane voltage drop after the 1st AP, measured from AP threshold.
3rd AP threshold	Analogous to *AP threshold* but for the 3rd AP.
3rd AP amplitude	Analogous to *AP amplitude* but for the 3rd AP.
3rd AP width	Analogous to *3rd AP width* but for the 3rd AP.
3rd AHP	Analogous to *AHP* but for the 3rd elicited AP.
*AP count**	Number of elicited APs in the current injection window $100-700$ *ms*.
*AP counts 1st 8th**	Number of elicited APs in $100-175$ *ms*.
*AP count 1st quarter**	Number of APs in $100-250$ *ms*.
*AP count 1st half**	Number of APs in $100-400$ *ms*.
*AP count 2nd half**	Number of APs in $400-700$ *ms*.
*AP amp adapt**	AP amplitude adaptation. 1st elicited *AP amplitude* divided by the amplitude of the 2nd elicited AP.
*AP average amp adapt**	AP average amplitude adaptation. Average ratio of all two consecutive AP heights as calculated by *AP amp adapt* during current injection window.
*AP CV**	Standard deviation divided by the mean of all AP amplitudes of APs elicited during the current injection window.
*ISI adapt**	Interspike interval (ISI) adaptation. ISI: time elapsed between two APs. ISI adapt: ratio of the 2nd ISI (between 2nd and 3rd elicited AP) to the 1st ISI (between 1st and 2nd elicited AP).
*ISI CV**	Standard deviation divided by the mean of all ISIs.
*Latency**	Time it takes to elicit the 1st AP, measured from current stimulation onset to *AP threshold*.
Rest V_m mean	Mean of the membrane voltage V_m before current stimulation onset $0-100$ *ms*. Also called resting membrane potential.
V_m mean	Mean of the membrane voltage V_m during current stimulation window $100-700$ *ms*.
V_m std	Standard deviation of the membrane voltage V_m during current stimulation window $100-700$ *ms*.
V_m skewness	Skewness of the membrane voltage V_m during current stimulation window $100-700$ *ms*.

Table 2 Description of 23 extracted electrophysiological features. *To make their distribution more Gaussian, these features are additionally log-transformed, except for the *AP average amp adapt* for which we used the *sigmoid* transform.

Task / Use	Link
Data and code	https://github.com/berenslab/mini-atlas
Read count data	https://github.com/berenslab/hh_sbi
Electrophysiological data	https://dandiarchive.org/dandiset/000008/
Electrophysiological features	https://github.com/berenslab/EphysExtraction
HH simulator: Brian2	https://brian2.readthedocs.io/en/stable/
Inference: SBI Toolbox[56]	https://www.mackelab.org/sbi/
tSNE: openTSNE	https://github.com/pavlin-policar/openTSNE
Parallel processing: Pathos[57]	https://mmckerns.github.io/project/pathos/wiki.html

Table 3 **Overview of all ressources used**

References

1. Zeng, H. & Sanes, J. R. Neuronal cell-type classification: challenges, opportunities and the path forward. *Nat. Rev. Neurosci.* **18**, 530–546 (2017).
2. Douglas, R. J., Martin, K. A. *et al.* Neuronal circuits of the neocortex. *Annu. review neuroscience* **27**, 419–451 (2004).
3. Harris, K. D. & Shepherd, G. M. The neocortical circuit: themes and variations. *Nat. neuroscience* **18**, 170–181 (2015).
4. Markram, H. *et al.* Reconstruction and simulation of neocortical microcircuitry. *Cell* **163**, 456–492 (2015).
5. Kepecs, A. & Fishell, G. Interneuron cell types are fit to function. *Nature* **505**, 318–326 (2014).
6. Tremblay, R., Lee, S. & Rudy, B. Gabaergic interneurons in the neocortex: from cellular properties to circuits. *Neuron* **91**, 260–292 (2016).
7. Gouwens, N. W. *et al.* Classification of electrophysiological and morphological neuron types in the mouse visual cortex. *Nat. neuroscience* **22**, 1182–1195 (2019).
8. Tasic, B. *et al.* Adult mouse cortical cell taxonomy revealed by single cell transcriptomics. *Nat. Neurosci.* **19**, 335 (2016).
9. Tasic, B. *et al.* Shared and distinct transcriptomic cell types across neocortical areas. *Nature* **563**, 72 (2018).
10. Zeisel, A. *et al.* Molecular architecture of the mouse nervous system. *Cell* **174**, 999–1014 (2018).
11. Yao, Z. *et al.* A transcriptomic and epigenomic cell atlas of the mouse primary motor cortex. *Nature* **598**, 103–110, DOI: 10.1038/s41586-021-03500-8 (2021).
12. Cadwell, C. R. *et al.* Electrophysiological, transcriptomic and morphologic profiling of single neurons using Patch-seq. *Nat. Biotechnol.* **34**, 199 (2016).
13. Cadwell, C. R. *et al.* Multimodal profiling of single-cell morphology, electrophysiology, and gene expression using Patch-seq. *Nat. Protoc.* **12**, 2531 (2017).
14. Fuzik, J. *et al.* Integration of electrophysiological recordings with single-cell rna-seq data identifies neuronal subtypes. *Nat. Biotechnol.* **34**, 175 (2016).
15. Lipovsek, M. *et al.* Patch-seq: Past, present, and future. *J. Neurosci.* **41**, 937–946 (2021).
16. Gouwens, N. W. *et al.* Integrated morphoelectric and transcriptomic classification of cortical gabaergic cells. *Cell* **183**, 935–953 (2020).
17. Scala, F. *et al.* Phenotypic variation of transcriptomic cell types in mouse motor cortex. *Nature* **598**, 144–150 (2021).
18. Kobak, D. *et al.* Sparse reduced-rank regression for exploratory visualization of paired multivariate data. *J. Royal Stat. Soc. Ser. C* (2021).
19. Bernaerts, Y., Berens, P. & Kobak, D. Sparse bottleneck neural networks for exploratory non-linear visualization of patch-seq data. *ArXiv* (2022).
20. Gala, R. *et al.* A coupled autoencoder approach for multi-modal analysis of cell types. In *Advances in Neural Information Processing Systems*, 9263–9272 (2019).
21. Gala, R. *et al.* Consistent cross-modal identification of cortical neurons with coupled autoencoders. *Nat. Comput. Sci.* **1**, 120–127 (2021).
22. Hodkgin, A. L. & Huxley, A. F. A quantitative description of membrane current and its application to conduction and excitation in nerve. *The J. Physiol.* **117**, 500–544 (1952).
23. Pospischil, M. *et al.* Minimal hodgkin-huxley type models for different classes of cortical and thalamic neurons. *Biol. Cybern.* **99**, 427–441, DOI: 10.1007/s00422-008-0263-8 (2008).
24. Hay, E., Hill, S., Schürmann, F., Markram, F. & Segev, I. Models of neocortical layer 5b pyramidal cells capturing a wide range of dendritic and perisomatic active properties. *PLOS Comput. Biol.* **7**, DOI: 10.1371/journal.pcbi.1002107 (2011).
25. Gonçalves, P. J. *et al.* Training deep neural density estimators to identify mechanistic models of neural dynamics. *eLife* **9**, DOI: 10.7554/eLife.56261 (2020).
26. Cranmer, K., Brehmer, J. & Louppe, G. The frontier of simulation-based inference. *PNAS* **117**, 30055–30062, DOI: 10.1073/pnas.1912789117 (2020).

27. Gouwens, N. W. *et al.* Systematic generation of biophysically detailed models for diverse cortical neuron types. *Nat. Commun.* **9**, DOI: 10.1038/s41467-017-02718-3 (2018).

28. Nandi, A. *et al.* Single-neuron models linking electrophysiology, morphology, and transcriptomics across cortical cell types. *Cell Reports* **40**, 111176, DOI: https://doi.org/10.1016/j.celrep.2022.111176 (2022).

29. Ward, D., Cannon, P., Beaumont, M., Fasiolo, M. & Schmon, S. M. Robust neural posterior estimation and statistical model criticism. In Oh, A. H., Agarwal, A., Belgrave, D. & Cho, K. (eds.) *Advances in Neural Information Processing Systems* (2022).

30. Cannon, P., Ward, D. & Schmon, S. M. Investigating the impact of model misspecification in neural simulation-based inference, DOI: 10.48550/ARXIV.2209.01845 (2022).

31. Schmitt, M., Bürkner, P.-C., Köthe, U. & Radev, S. T. Detecting model misspecification in amortized bayesian inference with neural networks, DOI: 10.48550/ARXIV.2112.08866 (2021).

32. Frazier, D. T., Drovandi, C. & Nott, D. J. Synthetic likelihood in misspecified models: Consequences and corrections, DOI: 10.48550/ARXIV.2104.03436 (2021).

33. Greenberg, D., Nonnenmacher, M. & Macke, J. Automatic posterior transformation for likelihood-free inference. In Chaudhuri, K. & Salakhutdinov, R. (eds.) *Proceedings of the 36th International Conference on Machine Learning*, vol. 97 of *Proceedings of Machine Learning Research*, 2404–2414 (PMLR, 2019).

34. Papamakarios, G. & Murray, I. Fast ε-free inference of simulation models with bayesian conditional density estimation. In Lee, D., Sugiyama, M., Luxburg, U., Guyon, I. & Garnett, R. (eds.) *Advances in Neural Information Processing Systems*, vol. 29 (Curran Associates, Inc., 2016).

35. Beck, J., Deistler, M., Bernaerts, Y., Macke, J. & Berens, P. Efficient identification of informative features in simulation-based inference. In *Advances in Neural Information Processing Systems* (Curran Associates, Inc., 2022).

36. Apicella, A. j. & Marchionni, I. Vip-expressing gabaergic neurons: Disinhibitory vs. inhibitory motif and its role in communication across neocortical areas. *Front. Cell. Neurosci.* **16**, DOI: 10.3389/fncel.2022.811484 (2022).

37. Traub, R. D. & Miles, R. *Neuronal networks of the Hippocampus* (Cambridge University Press, 1991).

38. Prinz, A. A., Bucher, D. & Marder, E. Similar network activity from disparate circuit parameters. *Nat. neuroscience* **7**, 1345–1352 (2004).

39. Deistler, M., Macke, J. H. & Gonçalves, P. J. Energy-efficient network activity from disparate circuit parameters. *Proc. Natl. Acad. Sci.* **119**, e2207632119 (2022).

40. Frazier, D. T. & Drovandi, C. Robust approximate bayesian inference with synthetic likelihood. *J. Comput. Graph. Stat.* **30**, 958–976, DOI: 10.1080/10618600.2021.1875839 (2021). https://doi.org/10.1080/10618600.2021.1875839.

41. Schölkopf, B. Causality for machine learning. In *Probabilistic and Causal Inference: The Works of Judea Pearl*, 765–804 (Association for Computing Machinery, 2022).

42. Buccitelli, C. & Selbach, M. mrnas, proteins and the emerging principles of gene expression control. *Nat. Rev. Genet.* **21**, 630–644 (2020).

43. Srivastava, H. *et al.* Protein prediction models support widespread post-transcriptional regulation of protein abundance by interacting partners. *PLOS Comput. Biol.* **18**, e1010702 (2022).

44. Schulz, D. J., Goaillard, J.-M. & Marder, E. E. Quantitative expression profiling of identified neurons reveals cell-specific constraints on highly variable levels of gene expression. *Proc Natl Acad Sci U S A* **104**, 13187–13191 (2007).

45. Zur, H. & Tuller, T. Predictive biophysical modeling and understanding of the dynamics of mrna translation and its evolution. *Nucleic acids research* **44**, 9031–9049 (2016).

46. Kotaleski, J. H. & Blackwell, K. T. Modelling the molecular mechanisms of synaptic plasticity using systems biology approaches. *Nat. Rev. Neurosci.* **11**, 239–251 (2010).

47. Holt, C. E., Martin, K. C. & Schuman, E. M. Local translation in neurons: visualization and function. *Nat. structural & molecular biology* **26**, 557–566 (2019).

48. Morisaki, T. & Stasevich, T. J. Quantifying single mrna translation kinetics in living cells. *Cold Spring Harb. perspectives biology* **10**, a032078 (2018).

49. Tutucci, E., Livingston, N. M., Singer, R. H. & Wu, B. Imaging mrna in vivo, from birth to death. *Annu. review biophysics* **47**, 85–106 (2018).

50. Stimberg, M., Brette, R. & Goodman, D. F. Brian 2, an intuitive and efficient neural simulator. *eLife* **8**, DOI: 10.7554/eLife.47314 (2019).

51. Colbert, C. M. & Pan, E. Ion channel properties underlying axonal action potential initiation in pyramidal neurons. *Nat. Neurosci.* **5**, 533–538, DOI: 10.1038/nn0602-857 (2002).

52. Yamada, W. M., Koch, C. & Adams, P. R. *Methods in neuronal modeling: From synapses to networks* (MIT press, 1989).

53. Rettig, J. *et al.* Characterization of a shaw-related potassium channel family in rat brain. *The EMBO journal* **11**, 2473–2486, DOI: j.1460-2075.1992.tb05312.x (1992).

54. Reuveni, I., Friedman, A., Amitai, Y. & Gutnick, M. Stepwise repolarization from ca2+ plateaus in neocortical pyramidal cells: evidence for nonhomogeneous distribution of hva ca2+ channels in dendrites. *J. Neurosci.* **11**, 4609–4621, DOI: 10.1523/JNEUROSCI (1993).

55. Jiang, B. Approximate bayesian computation with kullback-leibler divergence as data discrepancy. In Storkey, A. J. & Pérez-Cruz, F. (eds.) *International conference on artificial intelligence and statistics, AISTATS 2018*, vol. 84 of *Proceedings of machine learning research*, 1711–1721 (PMLR, 2018).

56. Tejero-Cantero, A. *et al.* sbi: A toolkit for simulation-based inference. *J. Open Source Softw.* **5**, 2505, DOI: 10.21105/joss.02505 (2020).

57. Michael M. McKerns, Leif Strand, Tim Sullivan, Alta Fang & Michael A.G. Aivazis. Building a Framework for Predictive Science. In Stéfan van der Walt & Jarrod Millman (eds.) *Proceedings of the 10th Python in Science Conference*, 76 – 86, DOI: 10.25080/Majora-ebaa42b7-00d (2011).

Acknowledgements

We thank Ziwei Huang for discussion. We thank the Deutsche Forschungsgemeinschaft (Heisenberg Professorship BE 5601/8-1 and Excellence Cluster 2064 “Machine Learning — New Perspectives for Science”, ref. 390727645) and the Federal Ministry for Education and Research (BMBF, FKZ 01IS18039A). The work was also funded by the European Union (ERC, “NextMechMod”, ref. 101039115). Views and opinions expressed are however those of the authors only and do not necessarily reflect those of the European Union or the European Research Council Executive Agency. Neither the European Union nor the granting authority can be held responsible for them. Additional support comes from the National Institute of Mental Health and National Institute of Neurological Disorders And Stroke under Award Number U19MH114830. The content is solely the responsibility of the authors and does not necessarily represent the official views of the National Institutes of Health. This work was also supported by the National Institutes of Mental Health grant UM1MH130981 and by the NIH under award number R01 MH109556.

Author contributions

Conceptualization, P.B., Y.B.; Methodology, Y.B., M.D., P.J.G., J.B., J.H.M., D.K., P.B.; Software, Y.B., M.S.; Formal Analysis, Y.B.; Data Curation, Y.B., F.S.; Writing – Original Draft, Y.B., P.B.; Writing – Review & Editing, all authors; Visualization, Y.B.; Supervision, A.S.T., J.H.M., D.K.,P.B.; Project Administration, P.B.; Funding Acquisition, A.S.T., J.H.M., P.B.

Declaration of Interests

The authors declare no competing interests.

SUPPLEMENTARY MATERIAL

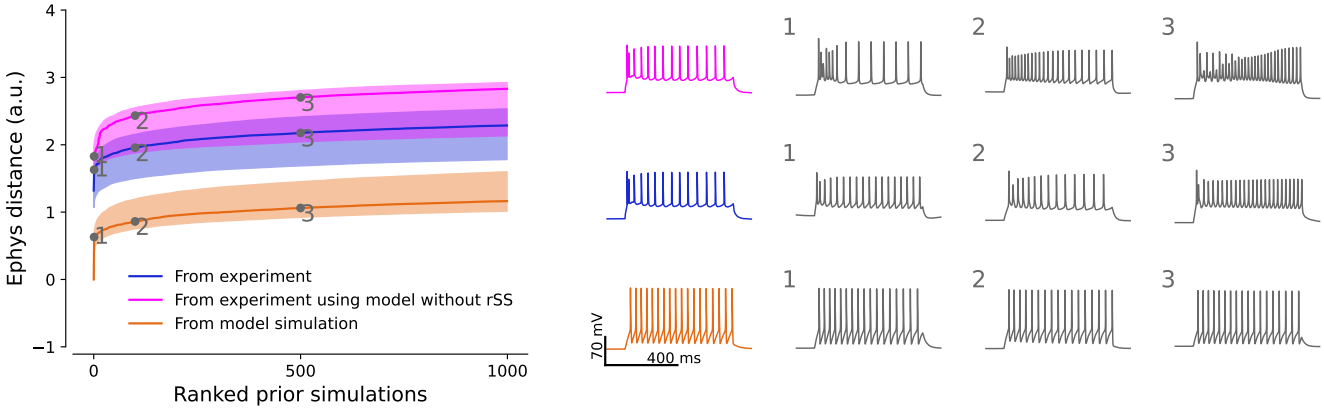

Figure S1 Model misspefication with and without scaling r_{SS} parameter. Analagous to Fig. 1d, but including model simulations without r_{SS} parameter.

Training schedule	MAP simulation fails (%)	$\|\mathbf{x_{MAP}} - \mathbf{x_o}\|_2$	10 random posterior draw simulation fails (%)	$\frac{1}{k}\sum_k \|\mathbf{x_k} - \mathbf{x_o}\|_2$
Standard **NPE**	12.77	6.24 ± 3.24	17.69	6.63 ± 3.24
Best Euclidean	14.14	5.11 ± 3.20	20.86	5.70 ± 3.36
Add 0.001 amplitude noise to ephys	7.33	5.36 ± 3.10	12.58	5.43 ± 3.17
Add 0.01 amplitude noise to ephys	5.86	4.81 ± 2.96	8.54	5.39 ± 3.11
add 0.05 amplitude noise to ephys	4.61	4.71 ± 2.98	9.01	5.34 ± 3.06
NPE-N: Add 0.1 amplitude noise to ephys	2.51	4.35 ± 2.86	6.22	5.11 ± 3.03
Add 1 amplitude noise to ephys	1.36	3.81 ± 2.11	7.27	5.19 ± 2.56
Add 0.05 amplitude noise to ephys and model parameters	3.66	5.42 ± 2.91	10.28	6.31 ± 2.86
Data augmentation	3.35	4.47 ± 2.98	6.98	4.91 ± 3.12
prior*	0.00	2.63 ± 0.81	52.29	11.79 ± 3.31

Table S1 Performance of various training schedules with NPE. 1st column Training schedules (see 4.5). **2nd column** Percentage of MAP simulation fails. A fail consists in having one or more undefined summary statistic. **3rd column** Distance of the MAP simulation $\mathbf{x_{MAP}}$ to the experimental reference $\mathbf{x_o}$ in standardized summary statistic space (mean $\pm$ SD over $n = 955$ MoP neurons). **4th column** Percentage of simulation fails corresponding to 10 randomly drawn HH model parameter combinations. **5th column** Average distance of simulations from $k = 10$ randomly drawn HH model parameter sets to the experimental reference in standardized summary statistic space (mean $\pm$ SD over $n = 955$ MoP neurons). *Regarding the prior, the MAP simulation is replaced by the prior simulation which has summary statistics closest to the experimental observation (2nd and 3rd column). In addition, 10 parameter combinations are randomly drawn from the prior (4th and 5th column).